



Modeling alpine grassland cover based on MODIS data and support vector machine regression in the headwater region of the Huanghe River, China

Jing Ge^a, Baoping Meng^a, Tiangang Liang^{a,*}, Qisheng Feng^a, Jinlong Gao^a, Shuxia Yang^a, Xiaodong Huang^a, Hongjie Xie^b

^a State Key Laboratory of Grassland Agro-ecosystems, Key Laboratory of Grassland Livestock Industry Innovation, Ministry of Agriculture and Rural Affairs, Engineering Research Center of Grassland Industry, Ministry of Education, College of Pastoral Agriculture Science and Technology, Lanzhou University, Lanzhou, 730000, PR China

^b Laboratory for Remote Sensing and Geoinformatics, Department of Geological Sciences, University of Texas at San Antonio, TX 78249, USA



ARTICLE INFO

Keywords:

Tibetan Plateau
Unmanned aerial vehicle
Pixel dichotomy model
Multivariate regression
Accuracy assessment
Trend analysis

ABSTRACT

Monitoring changes in grassland cover is essential in assessment of grassland health as well as the effects of anthropogenic interventions and global climate change on grassland ecosystems. Remote sensing is an effective approach for providing rapid and dynamic monitoring of vegetation cover over large grassland areas. In this study, four types of remote sensing retrieval models (i.e., pixel dichotomy models, univariate vegetation index (VI) regression models, multivariate regression models, and a support vector machine (SVM) model) are built to derive grassland cover based on moderate resolution imaging spectroradiometer (MODIS) data and the measured grassland cover data collected by unmanned aerial vehicle during the grassland peak growing season from 2014 to 2016. The optimal model is then used to map the spatial distribution of grassland cover and its dynamic change in the headwater region of the Huanghe River (Yellow River) (HRHR) of the northeastern Tibetan Plateau over the 16 years period (2001 to 2016). The results show that (1) the pixel dichotomy models based on MODIS VI data are inappropriate for estimating grassland cover in the HRHR when their endmembers (VI_{soil} and VI_{veg}) are determined based only on the MODIS data; (2) the multivariate regression models present better performance than the univariate VI (normalized difference vegetation index (NDVI) or enhanced vegetation index (EVI)) models; (3) MODIS NDVI outperforms MODIS EVI for modeling grassland cover in the study area; (4) the SVM model based on nine factors is the optimal model (R^2 : 0.75 and RMSE: 6.85%) for monitoring alpine grassland cover in the study area; and (5) majority of the grassland area (59.9%) of the HRHR showed increase in yearly maximum grassland cover from 2001 to 2016, while the average yearly maximum grassland cover for the 16 years exhibited a generally increasing trend from west to east and from north to south. This study provides a more suitable remote sensing inversion model to greatly improve the accuracy of modeling alpine grassland cover in the HRHR, and to better assess grassland health status and the impacts of warming climate to grasslands in regions of remote and harsh environments.

1. Introduction

Vegetation cover refers to the percentage of aboveground vegetation in relation to the total ground surface area (Purevdorj et al., 1998), and is a valuable parameter for reflecting vegetation growth status and a sensitive indicator of ecosystem change (Jiapaer et al., 2011). Monitoring vegetation cover of an extensive grassland is of great significance for assessing grassland resources and preventing grassland degradation. Accurate information on grassland cover status and changes can support government decisions regarding grassland management and livestock production (Wang et al., 2017; Purevdorj et al.,

1998). Remote sensing is the only available and effective approach for estimating grassland cover and monitoring its dynamic changes over a long time series in harsh environments of vast spatial extents. There are two approaches for deriving grassland cover based on satellite remote sensing data: spectral mixture analysis (SMA) and empirical model methods.

SMA provides an important method for deriving vegetation cover from multispectral and hyperspectral satellite data at a regional scale. Under this approach, each pixel in a satellite image is decomposed into a linear component of a reference spectrum, referred to as an end-member (Jiapaer et al., 2011; Elmore et al., 2000; Guerschman et al.,

* Corresponding author.

E-mail address: tgliang@lzu.edu.cn (T. Liang).

2009; Wu and Murray, 2003). The pixel dichotomy model is a simplified linear SMA model (Wittich and Hansing, 1995) that includes two vegetation index endmembers consisting of a VI_{veg} value from the 100% green vegetation area and a VI_{soil} value contributed by the bare soil area (Li et al., 2014; Qi et al., 2000; Gutman and Ignatov, 1998; Zeng et al., 2000). Due to its simplicity and interpretability, the pixel dichotomy model is rapid and effective in simulating dynamic changes in vegetation cover over a long time series at regional and even global scales. To the best of our knowledge, previous studies have concentrated on estimating sparse vegetation in arid and semiarid areas, and the selection of vegetation and non-vegetation endmembers has been based on satellite images with a 30 m or higher spatial resolution or *in situ* data (Li et al., 2014; Xiao and Moody, 2005; Liu et al., 2009; Jiapaer et al., 2011). However, at large regional scales, the utilization of high-resolution satellite images is constrained by high costs and weather conditions, and field surveys are further limited by additional factors. Moderate-resolution satellite images (e.g., MODIS imagery) may be more suitable for use at large regional scales because they present not only wide spatial coverage, but also a high temporal resolution. However, few studies have systematically evaluated the accuracy of pixel dichotomy models at a moderate spatial resolution (such as MODIS) in pastoral areas with relatively dense alpine grasslands, such as those found on the Tibetan Plateau (TP).

Empirical models have been widely adopted in recent years for determining vegetation cover. Good results have been achieved through establishing empirical relationships between satellite remote sensing and field-measured data, and then extrapolating vegetation cover estimates to a regional scale using such empirical formulas (Kergoat et al., 2015; Jakubauskas et al., 2000; North, 2002; Gitelson et al., 2002). The satellite data used in an empirical model can come from a single band, a combination of bands, or vegetation indices (VIs). Existing studies have shown that VIs are highly reliable and effective data sources for assessing vegetation cover. In this context, the normalized difference vegetation index (NDVI), enhanced vegetation index (EVI), ratio vegetation index, soil-adjusted vegetation index and modified soil-adjusted vegetation index have performed particularly well (Patel et al., 2007; Purevdorj et al., 1998; Rundquist, 2002; North, 2002; Lehnert et al., 2015). However, several existing studies have utilized empirical models based on a single VI without considering the ecological context and the spatial heterogeneity of grasslands. Moreover, each VI has its own limitations and uncertainties, which cause the models to produce good results only for the specified measurement areas while inappropriately describing the vegetation cover in other regions (Yang et al., 2017). Therefore, building multivariate models by adding other environmental factors (i.e., geographical location, terrain data and meteorological data) that are closely related to grassland cover is a more effective method that decreases the prediction error of single VI-based retrieval models and improves the stability and universality of grassland cover inversion models (Meng et al., 2018). Furthermore, according to different statistical methods, empirical models can be divided into categories including linear regression analysis (Zha et al., 2003; Psomas et al., 2011), nonlinear regression analysis (Gitelson et al., 2002), support vector machine (SVM) regressions (Schwieder et al., 2014; Lehnert et al., 2015), decision tree (DT) regressions (Hansen et al., 2002a, 2002b; Goetz et al., 2003), and artificial neural networks (ANN) (Boyd et al., 2002).

Compared to traditional linear and nonlinear regressions, the SVM method is a more advanced statistical method. SVM is a supervised and nonparametric machine learning algorithm that is used for classification and regression analyses (Vapnik et al., 1996). This method offers many unique advantages in coping with small samples and nonlinear and high dimensional pattern recognition, presenting a high correlation with predictor variables (Mountrakis et al., 2011; Verrelst et al., 2015). Schwieder et al. (2014) compared the capability of three machine learning models to estimate shrub vegetation cover and showed that all algorithms (SVM, partial least squares regression (PLSR), and random

forest regression) presented good predictive power, while the SVM model outperformed the others with an average R^2 value of 0.64 and a root mean square error (RMSE) of only 12%. Lehnert et al. (2015) obtained similar results when they studied the performance of four different methods (i.e., SVM, spectral angle mapper, PLSR, and linear spectral unmixing) used for estimating grassland cover on the TP, with an R^2 of up to 0.64, while RMSE was only 5.59% for the SVM model at the MODIS imagery scale.

Accurate field measurement data of grassland cover are important for developing and/or validating the two modeling approaches mentioned above. On the one hand, accurate measurement data are the basis for establishing high-quality empirical models. On the other hand, the results predicted by both pixel dichotomy models and empirical models need to be validated with accurate field-measured data (Zhou and Robson, 2001; Delamater et al., 2012). Field measurements are acquired by visual estimations, sampling, and photographic methods (Okin et al., 2013). These traditional measurement methods are generally conducted at a quadrat scale (i.e., 0.5 m × 0.5 m or 1 m × 1 m) and are often time consuming and labor intensive. Moreover, a major gap in spatial resolution exists between satellite remote sensing pixels and sample quadrats. Sampling representativeness is greatly influenced by the limited number and size of sampling quadrats, especially in complex natural grasslands with high spatial heterogeneity. Although substantially increasing the number of quadrats can solve this problem, a large number of quadrats implies larger consumption of time, manpower, and cost. This is therefore not suitable for sampling surveys over large areas, particularly in the Tibetan Plateau of high elevation and harsh environment. Unmanned aerial vehicle (UAV) is a powerful tool for effectively addressing the problem of spatial matching between surface ground measurements and satellite remote sensing due to the high resolution and large area coverage of UAV images (Rango et al., 2006; Salamí et al., 2014; Qin, 2014). Compared to satellite remote sensing, UAV images are collected closer to the ground, so the observation data are less disturbed by the atmosphere and other factors. UAVs also have the advantages of small size, light weight, low operating costs, convenient transportation, real-time image transmission and high flexibility, and can be employed to map vegetation cover in inaccessible areas by foot (Colomina and Molina, 2014; Yi et al., 2016; Capolupo et al., 2015). Rango et al. (2006, 2009) described the application of a UAV to acquire the canopy cover of woody vegetation in the experimental mixed rangeland of Jornada and obtained good results. Chen et al. (2016) used both the UAV photographic method and surface quadrat investigations to obtain fractional vegetation cover (FVC) data from alpine grassland of the Tibetan Plateau and then evaluated the accuracy of these two methods. The research ultimately reached the conclusion that the UAV provided more accurate FVC estimations at the pixel scale of satellite remote sensing image and was more effective than traditional surface measurements.

Therefore, utilizing MODIS VI data and grassland cover data collected by UAV, the objectives of this study are to (1) assess accuracy and applicability of different models (pixel dichotomy model, univariate linear and nonlinear regression, multivariate linear and nonlinear regression, and SVM regression) for alpine grassland cover inversion and (2) analyze the spatial distribution and temporal change in grassland cover over the peak growing season between 2001 and 2016 in the headwater region of the Huanghe River (HRHR) over Tibetan Plateau.

2. Data and methods

2.1. Study area

The HRHR (N33°02'58"–36°07'43", E95°53'47"–102°15'22") lies in northeastern TP (Fig. 1) and is a critical ecological barrier on the TP and one of the most important freshwater resources in China (Chu et al., 2016). The HRHR covers an area of approximately 105,190 km², with

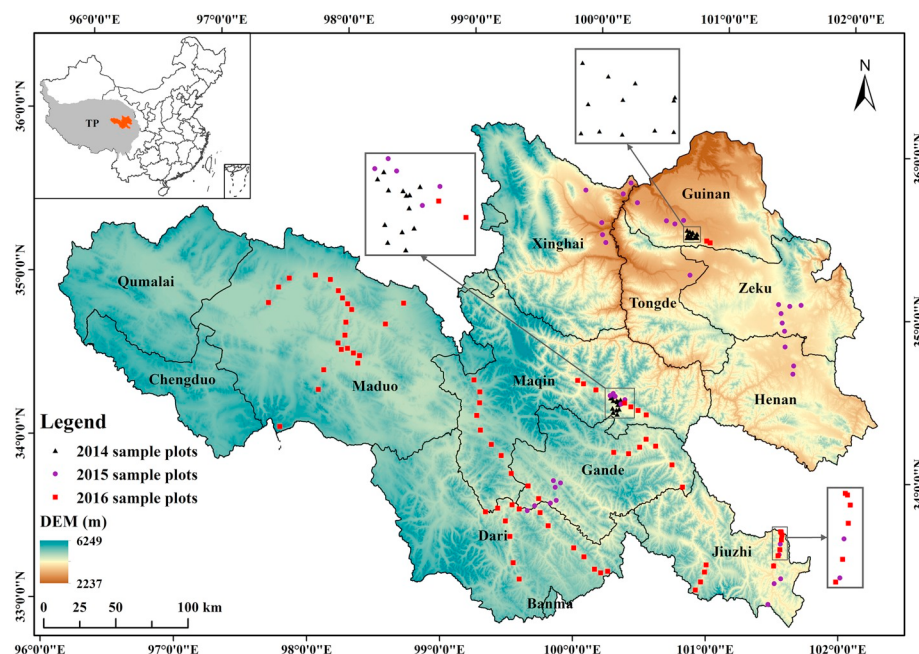


Fig. 1. DEM and locations of sample plot (100 m × 100 m) of grassland cover (obtained by unmanned aerial vehicle) from 2014 to 2016 in the headwater region of the Huanghe River (HRHR), Tibetan Plateau (TP), China. The three denser sample areas are enlarged (black boxes) to better show the sample plots.

an average elevation > 4000 m. As a result of the high elevation, the environmental conditions in this region are characterized by low annual temperatures, large diurnal temperature differences, seasonal precipitation extremes, intense evaporation, and strong solar radiation. The region is a fragile eco-environment and is sensitive to climate change (Li et al., 2016). The HRHR presents annual temperature between −4 °C and 2 °C, increasing from west to east. The total annual precipitation in the HRHR is approximately 420 mm, mostly from June to September (Li et al., 2016; Jin et al., 2011). The main types of land cover are grasslands, water, and barren lands (bare soil, abandoned land, saline-alkali soil, sands and gravel), with grasslands accounting for approximately 80% of the total land area. Grasslands play a vital role in protecting ecological environment and preventing land degradation (Zhou et al., 2005; Liu et al., 2006; Feng et al., 2005). The typical grassland vegetation consists of alpine shrub, alpine meadow and alpine steppe (Hu et al., 2017), and the soils are mainly alpine meadow and steppe soils (Yu et al., 2014).

2.2. Field data collection of grassland cover

Field survey data of grassland cover were collected by UAV during the peak growing season (July to September) from 2014 to 2016. Typical grassland vegetation communities with relatively flat terrain, uniform growth status, and spatially representative were selected as the sample plots, with size of 100 m × 100 m. The latitude, longitude, elevation, grassland type and dominant species were recorded for each plot. In total, 138 sample plots (25, 39, and 74 in 2014, 2015, and 2016, respectively) (Fig. 1) were sampled during the period from 2014 to 2016.

The UAV used was a Phantom 2 Vision + Quad-Rotor intelligent UAV (carrying a GoPro Hero 3+ digital camera) manufactured by DJI Innovations (DJI) (Shenzhen, China). A Naza-M GPS system assembled in Phantom 2 Vision + allows the horizontal position precision of the aircraft to reach ± 2.5 m (± 0.8 m vertically). The total number of effective pixels in the photographs captured by the GoPro Hero 3+ camera is 12 million (4000 × 3000) (Flynn and Chapra, 2014). With the locations of ground control points, the UAV could fly in autopilot mode at a specified height over a sample plot along a designed route, which was set up in the DJI VISION application (2014 and 2015) and

FragMAP software (2016) (Yi, 2017), thus increasing the security and controllability of UAV operation. In this study, the diagonal of the sample plot was selected as the flight route, and the UAV recorded aerial images every 3 s at nadir viewing, with a flight speed of 4 m/s. Flight height was set to approximately 30 m, at which height the ground resolution of each photograph is 1.2 cm, and a single aerial photograph can cover > 1728 m² (36 m × 48 m) of ground. Approximately 12 photographs were taken in each sample plot (100 m × 100 m), and it took only approximately 2 min for the UAV to complete a photography mission in a plot. The grassland cover of each photo is extracted using the photo analyzing module of FragMAP (Yi, 2017) (only taken 1–2 min per photo). The covers of the 12 photos are then averaged as the overall grassland cover of the plot. This grassland cover could be very close to the “true” cover of the entire plot and is much better than the average cover from the traditional method: five subplots of 0.5 m × 0.5 m (or 1 m × 1 m) size, one at the center and four at the corners (one at each corner) of the 100 m × 100 m plot.

2.3. MODIS data and processing

The VI data are derived from MODIS VI products (MOD13Q1) downloaded from a NASA data system (<https://earthdata.nasa.gov/>). The data in HDF format includes gridded NDVI and EVI products with a 250 m spatial resolution and 16-day temporal resolution. Two images, with orbit numbers h25v05 and h26v05, are needed to cover the entire study area. In total, 192 scenes from July to September are downloaded for the period of 2001 to 2016.

The processing of the MOD13Q1 data includes the following steps: (1) transforming and registering the MOD13Q1 data to Geo-Tiff format and Albers map projection using the MODIS Reprojection Tool (MRT), followed by extracting the NDVI and EVI images (the formulas employed for computing NDVI and EVI are shown in Table 1); (2) extracting the NDVI and EVI values of the 138 sample plots, covering the field sampling time of that year (Table 2); (3) calculating maximum NDVI (NDVI_{max}) and maximum EVI (EVI_{max}) datasets from July to September during 2001–2016; and (4) mosaicking two images with the same date of each year, and then clipping the mosaicked images using the vector HRHR boundary to serve as the data source for later simulating grassland cover over the 16-year period.

Table 1

Formulas and references for NDVI and EVI.

Variable	Formula	References
Normalized difference vegetation index (NDVI)	$(\text{Nir} - \text{Red}) / (\text{Nir} + \text{Red})$	Tucker et al., 1986; Huete et al., 1994
Enhanced vegetation index (EVI)	$2.5 \times (\text{Nir} - \text{Red}) / (\text{Nir} + C_1\text{Red} - C_2\text{Blue} + L)$	Huete et al., 1997; Huete et al., 2002

Note: Red, Nir and Blue represent the red, near-infrared and blue bidirectional surface reflectance; L is the soil-adjusted factor (equals to 1); C_1 and C_2 (equal to 6.0 and 7.5, respectively) are the aerosol resistance coefficients (Huete et al., 2002).

Table 2

Dates of NDVI/EVI and p/t matched with the field sampling times.

Field sampling time	Date of NDVI/EVI	Date of p/t
2014/08/19–2014/08/22	2014/08/13–2014/08/28	2014/01/01–2014/08/12
2015/08/01–2015/08/08	2015/07/28–2015/08/12	2015/01/01–2015/07/27
2016/07/30–2016/08/11	2016/07/27–2016/08/12	2016/01/01–2016/07/27

Note: NDVI/EVI represents the NDVI and EVI images from the MOD13Q1 products; p/t represents the interpolated precipitation/temperature dataset in this study.

Spatial grassland distribution data are acquired from the MODIS land cover product (MCD12Q1, V051) (<https://earthdata.nasa.gov/>) with the International Geosphere-Biosphere Programme (IGBP) scheme. The spatial resolution of these data is 500 m. MCD12Q1 data are converted from HDF to ESRI GRID format with Albers map projection using MRT software. In this study, the MCD12Q1 data from 2013 are reclassified into six categories using ArcGIS software according to the following scheme (Table 3). In addition, types 3 and 6 of the reclassified MCD12Q1 land cover data are extracted to represent the distribution of grasslands and bare soil in the HRHR, and the results are used to clip MOD13Q1 NDVI and EVI images to eliminate other land cover types; the clipped MOD13Q1 VI images are then served as the data source for the pixel dichotomy models.

2.4. Environmental factors and pre-processing

Shuttle Radar Topography Mission (SRTM) V4.1 data (Geo-TIFF format) are downloaded from the Geospatial Data Cloud (<http://www.gscloud.cn>). For this study, the SRTM digital elevation model (DEM) data are resampled from 90 m spatial resolution to 250 m to match the spatial resolution of the MOD13Q1 products, and the projection type is defined as Albers to extract the longitude, latitude, elevation, aspect and slope of each pixel over the extent of the study area using ArcGIS software.

The soil data (in Tiff format), including the sand concentrations and clay concentrations in 0–30 and 30–60 cm soil horizons, are derived from the China soil characteristics dataset (<http://globalchange.bnu.edu.cn/research/soil>) (Wei et al., 2012). The spatial resolution of the data is 1000 m, with Albers projection. We clip the soil data using the vector HRHR boundary for further analyses.

Table 3

Reclassified scheme of the MCD12Q1 land cover product.

Reclassify Type (New code)	Land cover type (IGBP Code)
Water bodies (1)	Water bodies (0)
Forest (2)	Evergreen needleleaf forest (1), Evergreen broadleaf forest (2), Deciduous needleleaf forest (3), Deciduous broadleaf forest (4), Mixed forest (5), Closed shrublands (6)
Grasslands (3)	Open shrublands (7), Woody Savannas (8), Savannas (9), Grasslands (10), Permanent wetlands (11)
Artificial surfaces (4)	Croplands (12), Urban and built-up (13), Cropland mosaics (14)
Permanent snow and ice (5)	Snow/Ice (15)
Barren or sparsely vegetated (6)	Barren or sparsely vegetated (16)

Meteorological data of 2001 to 2016 are downloaded from the China Meteorological Data Sharing Service System (<http://data.cma.cn>), including daily precipitation and the daily average temperature from 149 meteorological stations on the TP and in surrounding areas. To match the temporal resolution of the meteorological data to that of the MOD13Q1 products, the daily precipitation are accumulated and the daily temperature are averaged every 16 days, corresponding to 16-day periods of MOD13Q1 products. These calculated data are used for spatial interpolation with professional interpolation software (ANUSPLIN, version 4.36) developed by Australian National University. The ANUSPLIN package was designed to fit the surface of climate data using thin plate smoothing splines; we select 250 m spatial resolution and Albers projection during the interpolation. When fitting surfaces to precipitation, there are three independent spline variables: longitude, latitude and elevation above sea level. In the case of fitting the temperature surface, the elevation is used as an independent covariate instead of a third independent spline variable; thus, an elevation linear sub-model is introduced. This is a robust way of allowing for dependence of the temperature on elevation (Mbogga et al., 2009; Price et al., 2000; McVicar et al., 2007). In addition, the coefficients of the sub-models can be interpreted as temperature lapse rates that are automatically determined according to the input data (Hutchinson, 2006). The interpolated results are clipped using the vector HRHR boundary to obtain the spatial climate datasets for the HRHR. The values of precipitation (p) and temperature (t) are extracted for the 138 sample plots (cells) from the interpolated climate datasets whose dates are shown in Table 2.

2.5. Construction and evaluation of grassland cover inversion models

In this study, the grassland cover is modeled with four types of models: pixel dichotomy models, univariate VI regression models, multivariate regression models, and an SVM model. According to the 80/20 rule (i.e., Pareto principle) (Benoit and Van den Poel, 2009; Yu, 2011), the data from 138 sample plots are first divided into two parts in an 80:20 ratios (i.e., 110 sample plots for training dataset and 28 for test dataset). The 110 training sample data randomly selected in MATLAB (R2016a) are used to establish the univariate VI regression models, multivariate regression models, and SVM model (Vapnik et al., 1996); the remaining 28 test sample data are served to validate the accuracy of all models.

2.5.1. Pixel dichotomy model

Pixel dichotomy model assumes that the linear, proportion-weighted combination of VI values from bare soil and green vegetation,

respectively, contribute to the total VI value in a pixel of an image (Liu et al., 2009; Xiao and Moody, 2005). Following this principle, a VI pixel observed by remote sensors can be marked as VI_{veg} for green vegetation information and VI_{soil} for bare soil information (Zribi et al., 2003). Hence, the expression of pixel dichotomy model for estimating vegetation cover (VC) is.

$$VC = (VI - VI_{soil}) / (VI_{veg} - VI_{soil}) \quad (1)$$

where VI_{soil} is the pure pixel VI value of bare soil; and VI_{veg} represents the VI value of a 100% vegetation pixel.

According to the Eq. (1), the pixel dichotomy model based on NDVI or EVI for estimating VC (denoted as VC_N and VC_E) is defined as

$$VC_N = (NDVI - NDVI_{soil}) / (NDVI_{veg} - NDVI_{soil}) \quad (2)$$

$$VC_E = (EVI - EVI_{soil}) / (EVI_{veg} - EVI_{soil}) \quad (3)$$

where $NDVI_{soil}$ (EVI_{soil}) and $NDVI_{veg}$ (EVI_{veg}) are the NDVI (EVI) values of a pure pixel for bare soil and a pure pixel with 100% vegetation coverage, respectively (Carlson and Ripley, 1997).

Ideally, $NDVI_{soil}$ or EVI_{soil} values are close to 0, and $NDVI_{veg}$ or EVI_{veg} values are close to 1, but the VI_{soil} value often varies from -0.1 to 0.2 under the influence of some factors (Carlson and Ripley, 1997). In addition, $NDVI_{veg}$ or EVI_{veg} values also change in different spaces and at different times (Kaufman and Tanré, 1992; Rundquist, 2002). In practice, endmember values can be directly determined through VI remote sensing images, or pure pixels are identified depending on field-measured data. For example, Zribi et al. (2003) regarded the $NDVI_{min}$ and $NDVI_{max}$ within a given confidence interval of an NDVI remote sensing image as the $NDVI_{soil}$ and $NDVI_{veg}$, respectively. Liu et al. (2009) calculated the cumulative NDVI percentage of an image and selected the corresponding NDVI values of the 1% and 99% cumulative percentages as the $NDVI_{soil}$ and $NDVI_{veg}$ values, respectively. In a study by Li et al. (2014), the VI endmember values were derived from field-measured spectral data. In our study, considering the absence of field-measured endmember data and the inevitable noise of satellite images, 0.5% and 99.5% are selected as the endmembers of the NDVI and EVI cumulative percentages, and the corresponding VI values of the 0.5% and 99.5% cumulative percentages are regarded as the VI_{soil} (0.5%) and VI_{veg} (99.5%) values.

2.5.2. Regression analysis

To analyze the correlation between grassland cover and NDVI or EVI, linear, logarithmic, power and exponential univariate VI models are structured. However, NDVI or EVI is not the only factor reflecting grassland cover, as other environmental factors (e.g., geographical location, topography, soil, and climate) are also closely related to grassland cover (Liang et al., 2016; Li and Guo, 2014; Wang et al., 2001; Beurs and Henebry, 2004; O'Connor et al., 2001; Gao et al., 2013). Therefore, linear, logarithmic, power and exponential multivariate regression models (Eqs. (4), (5), (6), and (7)) are respectively constructed in SPSS 16.0 to explore the relationships between grassland cover and all of the abovementioned factors. Moreover, 13 variables are screened for multivariate regression models, including position and terrain (longitude, latitude, elevation, aspect and slope), edaphic (0–30 m sand, 0–30 cm clay, 30–60 cm sand and 30–60 cm clay concentrations), meteorological (precipitation and temperature) and VIs (MOD13Q1 NDVI and EVI) factors. Among them, these factors reaching the extremely significant correlation with grassland cover, as determined by the F test, are applied in the construction of the multivariate models.

$$y = \beta_0 + \beta_1 x_1 + \beta_2 x_2 + \dots + \beta_i x_i + \varepsilon \quad (4)$$

$$y = \beta_0 + \beta_1 \ln x_1 + \beta_2 \ln x_2 + \dots + \beta_i \ln x_i + \varepsilon \quad (5)$$

$$y = \beta_0 x_1^{\beta_1} x_2^{\beta_2} \dots x_i^{\beta_i} e^{\varepsilon} \quad (6)$$

$$y = \beta_0 e^{\beta_1 x_1} e^{\beta_2 x_2} \dots e^{\beta_i x_i} e^{\varepsilon} \quad (7)$$

where y is grassland cover; the selected independent variables are x_1 , x_2 , ..., x_i , β_0 , β_1 , β_2 ..., β_i represent the parameters of the model; and ε represents the error term.

There are two important reasons why SVM regression is selected to estimate grassland cover in our study. One reason is that SVM regression achieves a good balance between overfitting and prediction accuracy. The other and more important reason is the SVM model's insensitivity to the sample size of the training dataset; that is, it can produce comparable accuracy with much smaller training sample sizes than alternative methods such as DT or ANN (Mountrakis et al., 2011; Foody and Mathur, 2004; Camps-Valls et al., 2006). To further confirm that the SVM model performs better than traditional linear and non-linear regression models in estimating grassland cover, the same training and test datasets are used to construct SVM model based on the same factors used in multivariate regression models. The SVM regression is implemented in MATLAB (R2016a) based on the "LIBSVM" package developed by Professor Lin and others from National Taiwan University (Chang and Lin, 2011). The type of the SVM model is epsilon-SVR (support vector regression), and the radial basis function (RBF) is the selected kernel function.

2.5.3. Model evaluation indices

The fitness of the models is measured by the coefficient of determination (R^2) of training dataset, and the prediction accuracy evaluation indices are as follows: correlation coefficient (r), RMSE (Eq. (8)), and coefficient of variation of the root mean square error (CVRMSE) (Eq. (9)) (Rinaldi et al., 2003; Loague and Green, 1991).

$$RMSE = \sqrt{\frac{\sum_{i=1}^n [E(y_i) - y_i]^2}{n}} \quad (8)$$

where $E(y_i)$ and y_i are the predicted and measured values of response y for observation i , respectively, and n equals the sample size (here $n = 28$). The lower the RMSE is, the higher the model accuracy is (Olden and Jackson, 2000).

$$CVRMSE (\%) = \sqrt{\frac{\sum_{i=1}^n [y_i - \hat{y}_i]^2}{n}} \times \frac{100}{\bar{y}} \quad (9)$$

where \bar{y} is the measured mean value; y_i and \hat{y}_i are the predicted and measured values of response y for observation i , respectively; and n equals the sample size (here $n = 28$). If $CVRMSE > 30\%$, the model predictive power is poor; when $CVRMSE$ varies from 20 to 30%, it is just fair; if $CVRMSE$ is 10–20%, the predictive capability is good; and when $CVRMSE < 10\%$, the predictive power can be excellent (Pan et al., 2006; Jamieson et al., 1991).

2.6. Spatial distribution and dynamic change in grassland cover

The yearly maximum grassland covers (i.e., maximum cover from July to September) at the scale of study area for the 16 years (2001 to 2016) are simulated using the optimal model and the spatial datasets of independent variables required by the optimal model. These grassland cover datasets are then averaged to obtain the spatial distribution map of the average yearly maximum grassland cover over the 16 years in the HRHR.

The temporal change in yearly maximum grassland cover from 2001 to 2016 is analyzed with a linear trend model of the slope (Fensholt et al., 2009; Stow et al., 2004). The model is characterized by simplicity and robustness. The vegetation cover change in each pixel could be simulated with the model, and the change in grassland cover is thereby extrapolated to the entire study area (Zhao et al., 2015; Dai et al., 2011). When the slope is $> 0\%/\text{yr}$, the grassland cover shows an increasing trend; otherwise, the inverse is true. The slope equation is

$$\text{slope} = \frac{n \times \sum_{i=1}^n i \times \text{cover}_i - \sum_{i=1}^n i \sum_{i=1}^n \text{cover}_i}{n \times \sum_{i=1}^n i^2 - (\sum_{i=1}^n i)^2} \quad (10)$$

where n equals to the total number of years (16); i is a number from 2001 to 2016 (i.e., 1–16); and cover_i is the yearly maximum grassland cover simulated from the selected optimal model in the i -th year.

To further analyze the significance of temporal change in grassland cover, we introduce the F test (Song et al., 2010). If $F > F_{0.05}(1, n-2)$, the change is significant at the 95% confidence level; here $F_{0.05}(1, 14) = 4.60$. According to this rule, the F test in each pixel is calculated. By overlaying the slope and the F test datasets, the change in grassland cover in entire study area is classified into four categories: significantly increasing ($\text{slope} > 0\%/\text{yr}$ and $F > 4.60$), increasing ($\text{slope} > 0\%/\text{yr}$ and $F < 4.60$), decreasing ($\text{slope} < 0\%/\text{yr}$ and $F < 4.60$) and significantly decreasing ($\text{slope} < 0\%/\text{yr}$ and $F > 4.60$). The F test is expressed as

$$F = \frac{R^2(n-2)}{1-R^2} \quad (11)$$

$$r = \frac{\sum_{i=1}^n (i - \bar{i})(\text{cover}_i - \bar{\text{cover}})}{\sqrt{\sum_{i=1}^n (i - \bar{i})^2 \sum_{i=1}^n (\text{cover}_i - \bar{\text{cover}})^2}} \quad (12)$$

where n equals to the total number of years (16); R^2 is the square of correlation coefficient (r) between the cover in each pixel and the time series; \bar{i} is the average of number 1–16 and it equals to 8.5 in this case; cover_i is the yearly maximum grassland cover, simulated from the selected optimal model for the i -th year; and $\bar{\text{cover}}$ is the average yearly maximum grassland cover from 2001 to 2016.

3. Results

3.1. Descriptive statistics of NDVI, EVI and grassland cover from 2014 to 2016

The statistical results (Table 4) show that the UAV-derived grassland cover data ranges from 26.37% to 99.00%, and the coefficient of variation (CV) is 20.57%, revealing great differences in the 138 sample plots during the grassland peak growing season. MODIS-derived NDVI and EVI show similar results as the grassland cover, ranging from 0.21 to 0.84 (0.63 difference) and 0.15 to 0.76 (0.61 difference), respectively, with the NDVI presenting a wider range. The overall maximum (Max), minimum (Min) and average (Avg) values of NDVI are all higher than the corresponding EVI values (10.53%, 40.00%, and 41.86% higher, respectively). The dispersion level of the NDVI is lower than that of EVI data according to the CV, which are 25.73% and 30.29%, respectively. The total average values of grassland cover, NDVI, and EVI are 81.04%, 0.61, and 0.43, respectively. In particularly, the minimum values of three indices are all found in the country Maduo, while the maximum values are in different counties.

Table 4

Statistics of UAV-derived grassland cover, MODIS-derived NDVI and EVI from 2014 to 2016 in the HRHR ($n = 138$).

County	Samples	Cover (%)				NDVI				EVI			
		Max	Min	Avg	CV (%)	Max	Min	Avg	CV (%)	Max	Min	Avg	CV (%)
Banma	1	78.11	78.11	78.11	–	0.66	0.66	0.66	–	0.46	0.46	0.46	–
Dari	21	96.33	47.70	83.76	14.26	0.79	0.53	0.66	11.43	0.63	0.31	0.48	16.02
Gande	11	97.35	52.27	77.20	16.14	0.83	0.52	0.67	12.07	0.76	0.37	0.50	19.87
Tongde	1	53.61	53.61	53.61	–	0.48	0.48	0.48	–	0.31	0.31	0.31	–
Guinan	20	99.00	44.75	90.65	14.22	0.80	0.45	0.71	13.89	0.62	0.26	0.48	21.22
Henan	3	98.50	96.50	97.64	1.06	0.77	0.75	0.76	1.63	0.64	0.60	0.62	3.35
Jiuzhi	16	97.51	76.66	92.38	6.81	0.84	0.62	0.72	9.36	0.63	0.37	0.49	15.98
Maduo	22	89.44	26.37	62.07	29.37	0.59	0.21	0.35	31.83	0.42	0.15	0.24	29.90
Maqin	33	99.00	57.59	83.56	14.38	0.80	0.28	0.62	18.66	0.64	0.20	0.45	22.29
Xinghai	4	63.38	34.58	51.90	24.22	0.54	0.33	0.44	20.02	0.29	0.18	0.24	19.37
Zeku	6	96.92	78.56	88.17	6.96	0.78	0.70	0.74	3.53	0.62	0.48	0.56	9.57
Total	138	99.00	26.37	81.04	20.57	0.84	0.21	0.61	25.73	0.76	0.15	0.43	30.29

Table 5

Assessment of the pixel dichotomy models of grassland cover based on NDVI or EVI.

Vegetation index	Cover (%)		
	RMSE (%)	r	CVRMSE (%)
NDVI	17.53	0.75	21.31
EVI	22.99	0.71	27.95

Note: CVRMSE is the coefficient of variation of the root mean square error (RMSE).

3.2. Assessment of the pixel dichotomy models

Table 5 shows the relationships between the values predicted by the pixel dichotomy models and the measured grassland cover values for the 28 samples in the test dataset. The result indicates that the NDVI-based pixel dichotomy model performs better than the EVI-based model, in all evaluation indices. The NDVI-based model, however, as indicated by the CVRMSE value (21.31%), is only a fair model of predictive power (i.e., between 20% and 30%).

3.3. Assessment of the univariate VI regression models

Comparing Tables 6 and 5, it is clear that univariate VI regression models perform far better than the pixel dichotomy models, in all evaluation indices. Overall, similar as the pixel dichotomy models, the NDVI-based regression models outperform the EVI-based regression models. Among the NDVI-based regression models (Table 6), the linear model has the optimal performance, while the logarithmic model is the best among all EVI-based regression models (both shown in Fig. 2). In terms of predictive capability, the CVRMSE values of all univariate regression models are in the range of 10% to 20%, showing good predictability.

3.4. Assessment of the multivariate regression models

The results of the F test for the linear models established by each factor (independent variable) and grassland cover (dependent variable) are shown in Table 7, which indicates that NDVI presents the highest correlation with grassland cover ($r = 0.81$). Overall, nine factors are extremely significantly related to grassland cover, including longitude (X), elevation (h), slope (S), 0–30 cm sand content (s1), 30–60 cm sand content (s2), precipitation (p), temperature (t), NDVI and EVI. Among these factors, X, S, t, p, NDVI and EVI show positive correlations with grassland cover while h, s1 and s2 are negatively correlated with grassland cover, in agreement with the previous studies (Li and Guo,

Table 6

Assessment of the univariate regression models of grassland cover based on NDVI or EVI.

Vegetation index	Model	Training dataset (n = 110)	Test dataset (n = 28)		
			R ²	RMSE (%)	r
NDVI	Linear	0.65	10.31	0.80	12.53
	Logarithmic	0.63	10.78	0.79	13.11
	Power	0.65	10.56	0.80	12.84
	Exponential	0.64	10.35	0.80	12.58
EVI	Linear	0.60	11.27	0.76	13.70
	Logarithmic	0.63	11.03	0.77	13.41
	Power	0.62	11.19	0.77	13.60
	Exponential	0.56	11.70	0.74	14.22

Note: All models meet the conditions for $P < 0.001$.

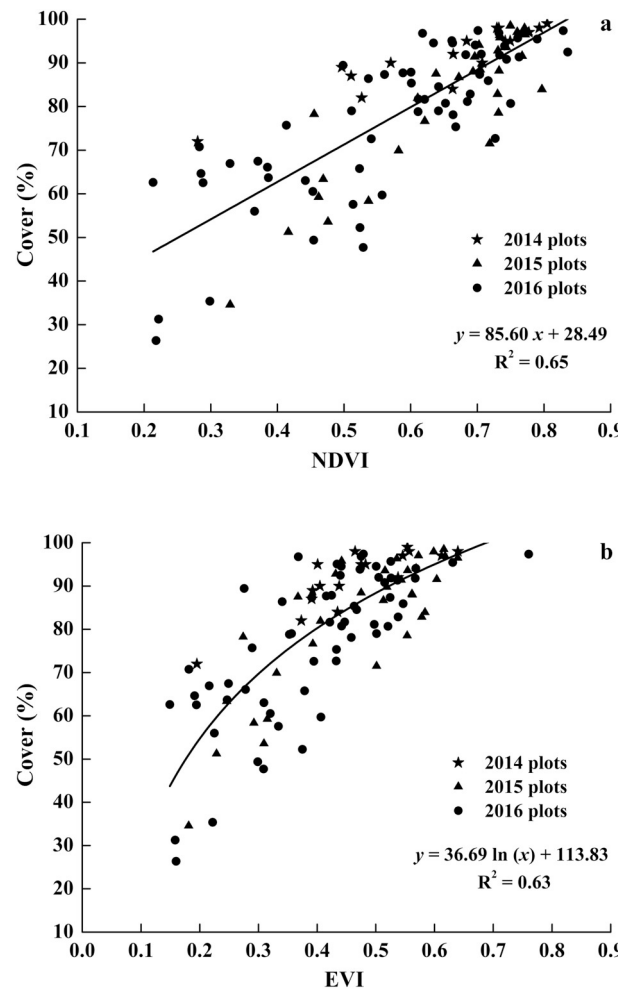


Fig. 2. Optimal univariate VI regression models of grassland cover based on NDVI (a) or EVI (b).

2014; Wang et al., 2001; Beurs and Henebry, 2004; O'Connor et al., 2001; Gao et al., 2013). The above nine factors are selected for use in building the multivariate models.

Comparing Tables 8 and 6, both the model fitting and retrieval accuracy for grassland cover based on the multivariate regression models are better than those based on the univariate VI models, and the multivariate regression models show similar but slightly better predictive power, as indicated by the values of CVRMSE. Among the four

multivariate regression models (Table 8), the linear model is recognized as the optimal model according to all evaluation indices, and it is expressed as

$$y = -564.33 - 2.52 \times X + 0.02 \times h + 0.21 \times S - 0.45 \times s1 + 0.36 \times s2 + 0.01 \times p + 2.85 \times t + 72.80 \times \text{NDVI} + 31.33 \times \text{EVI} \quad (13)$$

where y is grassland cover (%); X , h , S , $s1$, $s2$, p , and t are the longitude, elevation, slope, 0–30 cm sand content, 30–60 cm sand content, precipitation and temperature, respectively.

3.5. Assessment of the SVM regression model

As shown in Table 9, the SVM model shows high inversion accuracy of grassland cover and can reflect 75% of the change in grassland cover (Fig. 3a), which is better than the multivariate regression models (Table 8). The R^2 increased by 0.07–0.09, and the RMSE values are prominently decreased by 27.21–31.98% as compared with multivariate regression models. The CVRMSE (equals to 8.09%) of the SVM model is < 10%, showing an excellent predictive capability. The results explain that the inversion values of the SVM model developed in this study are very close to the field-measured grassland cover values ($r = 0.88$) (Fig. 3b), and it is clear that the SVM model outperforms other models. Hence, the SVM model is identified as the optimal model in this study and is used to obtain the spatial distribution and dynamic change of grassland cover throughout the HRHR. A detailed list of the SVM model structure is shown in Table 10.

3.6. Spatial distribution and trend analysis of grassland cover based on the SVM model

The yearly maximum grassland covers (i.e., maximum cover from July to September) at the scale of study area over the 16 years (2001 to 2016) are simulated using the SVM model (the optimal model in this study). Fig. 4 illustrates the average result for yearly maximum grassland cover for the 16 years. The result shows that high grassland cover was mainly centered in the eastern study area, possibly because the eastern area is the main pastoral area with higher precipitation and temperature in the HRHR. The northern parts of Qumalai, Maduo and Xinghai showed a low grassland cover distribution, which may be resulted from the higher elevation (Fig. 1). However, the triangle zone of Xinghai, Guinan and Tongde presented lower elevation and low cover. This is reasonable, considering the high population densities in these areas, and the strong disturbances of grasslands caused by frequent human activities. In general, the spatial distribution of the average yearly maximum grassland cover exhibited an increasing trend from west to east and from north to south. This is consistent with the annual precipitation that had similar spatial change as the grassland cover; meanwhile, the annual temperature increased gradually from west to east, showing the consistent change trend in the longitude as grassland cover (Li et al., 2016; Jin et al., 2011). In addition, precipitation and temperature are positively related to grassland cover in the HRHR (Table 7). Therefore, the spatial change in grassland cover in this area may be greatly affected by precipitation and temperature together.

As shown in Fig. 5, over the past 16 years, 7.3% of grassland area showed significant increase (at 95% confidence level) in grassland cover. These areas were mainly located in the triangle zone of Xinghai, Guinan and Tongde, a low grass cover area (Fig. 4). There were also significant increases in the central region of Maduo and parts of Qumalai and Dari. Only 2.5% of the grassland area showed significant decrease in grassland cover. These areas were mainly located in the middle of Qumalai, with scattered small areas across Chengduo, Maduo and Guinan. 52.6% of the grassland area showed increase, primarily distributed in Maduo and Dari counties and the far west of Maqin and the marginal zone of Xinghai. The grassland area showed a 37.6% decrease, mainly in the western Henan, the eastern Maqin and Gande, the

Table 7

F test of linear regression models between each factor (x) and grassland cover (y) ($n = 138$).

Main factor	Independent variable	Model formula	r	F
Geographic location and topography	Longitude (°)	$y = 8.04 x - 723.15$	0.53	51.76**
	Latitude (°)	$y = -4.05 x + 220.47$	-0.17	4.09
	Elevation (m)	$y = -0.01 x + 137.61$	-0.28	11.95**
	Slope (°)	$y = 1.65 x + 74.94$	0.33	16.37**
Soil	Aspect (°)	$y = -0.03 x + 85.69$	-0.19	4.98
	0–30 cm sand content (%)	$y = -0.51 x + 98.96$	-0.35	19.09**
	0–30 cm clay content (%)	$y = 0.09 x + 79.64$	0.02	0.06
	30–60 cm sand content (%)	$y = -0.36 x + 91.08$	-0.32	15.50**
Meteorology	30–60 cm clay content (%)	$y = 0.35 x + 73.53$	0.09	1.04
	precipitation (mm)	$y = 0.10 x + 53.71$	0.43	31.41**
	temperature (k)	$y = 2.92 x - 717.74$	0.30	13.91**
Vegetation index	NDVI	$y = 85.05 x + 28.88$	0.81	250.87**
	EVI	$y = 97.61 x + 38.62$	0.77	199.01**

Note: r is the correlation coefficient between each factor (x) and grassland cover (y).

** $P < 0.001$.

Table 8

Assessment of the multivariate regression models of grassland cover.

Model	Training dataset ($n = 110$)		Test dataset ($n = 28$)	
	R ²	RMSE (%)	r	CVRMSE (%)
Linear	0.68	9.41	0.84	11.44
Logarithmic	0.68	10.07	0.82	12.25
Power	0.67	9.54	0.83	11.60
Exponential	0.66	9.59	0.83	11.66

Note: All models meet the condition for $P < 0.001$.

Table 9

Assessment of the SVM regression model of grassland cover.

Model	Training dataset ($n = 110$)		Test dataset ($n = 28$)	
	R ²	RMSE (%)	r	CVRMSE (%)
SVM	0.75**	6.85	0.88	8.09

** $P < 0.001$.

southern Xinghai and Tongde, and most of Jiuzhi. Interestingly, these areas are the high grassland cover areas as shown in Fig. 4. Overall, the yearly maximum grassland cover increased in most area (59.9%) of the HRHR from 2001 to 2016. This was partially due to a series of related programs and measures implemented in recent years that focused on comprehensive control and restoration of grasslands, such as the “Rangeland to Grassland” (*tuimu huancao*), “China's Western Development” (*xbu dakaifa*), “Four Ways Program” (*sipeitao jianshe*), and “Poverty Alleviation through Migration” (*yimin fupin*) (Bauer and Nyima, 2011; Yeh, 2005). In addition, the temporal change in grassland cover may also be affected by the warm and wet trends of climate in the HRHR in the last twenty years (Jin et al., 2011; Hu et al., 2012).

4. Discussion

4.1. Limitations of the pixel dichotomy model

As mentioned in the introduction, the pixel dichotomy model is simple and interpretable and can rapidly simulate dynamic changes in vegetation cover over a long time series. However, the selection of endmembers is critical to the success of the pixel dichotomy model. Qi et al. (2000) demonstrated that the pixel dichotomy model could provide a reasonable estimate of vegetation dynamics at a regional scale using Landsat TM imagery (30 m resolution), in which the VI endmembers were directly derived from the Landsat TM images. Xiao and Moody (2005), classified a high-resolution (0.3 m) orthoimage into

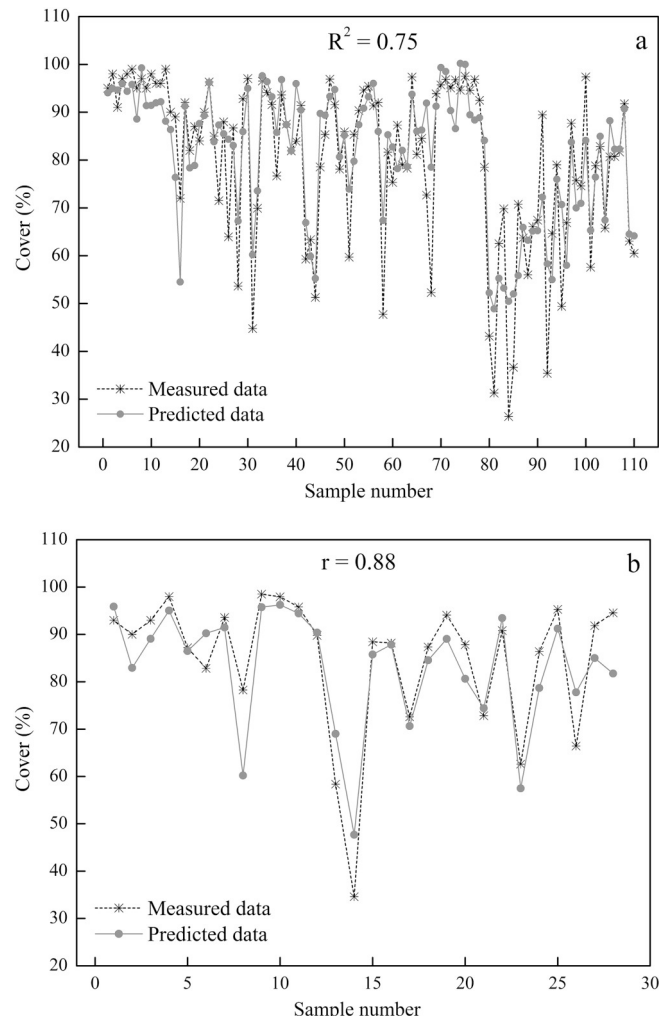


Fig. 3. Relationships between the predicted grassland cover and the measured grassland cover in the training dataset (a) and test dataset (b) based on the SVM regression model.

green vegetation, non-green vegetation and soil parts based on Bayesian maximum likelihood classification, and the classification results were used to derive endmember values in an ETM+ image (30 m resolution). Finally, they proved that the NDVI-based pixel dichotomy model presented good accuracy ($R^2 = 0.88$, RMSE = 11%) when estimating the vegetation fraction in a transition zone from desert to upland in New

Table 10

Structure of the SVM regression model of grassland cover.

Parameter	Value
SVM type	epsilon-SVR
Kernel function type	radial basis function (RBF)
Kernel coefficient gamma for RBF	0.088
Penalty factor C of the error term	2
Epsilon	0.1
Tolerance for stopping criterion	1e-3
Kernel cache size	100 MB

Mexico. However, due to low coverage and serious effects from clouds, high-resolution images cannot practically be used to achieve macroscopic monitoring of large-scale vegetation cover; thus, we believe that moderate-resolution satellite imagery (e.g., MODIS imagery with a 250 m resolution) may be a better choice. Field-measured VI end-member values are conducive to improving the estimation accuracy in the pixel dichotomy model. But in our study area, it is unfortunately almost impossible to find enough number of 250 m × 250 m of pure bare soil or vegetation-covered sampling plots corresponding to MODIS image pixels in the field. Therefore, we determine the VI endmembers by using confidence intervals or the cumulative percentages of a VI image. As far as this method is concerned, the problem still exists because the endmember values in this method are empirical and are mainly determined by the size and sharpness of the images, the growth status of vegetation, and other factors (Qi et al., 2000). Therefore, it is difficult to judge whether the selection of endmember values is appropriate or not. Thus, this method increases the uncertainty of the pixel dichotomy model, which could explain why the accuracy of the pixel dichotomy model is not found to be satisfactory when compared with other models in our study. In summary, there are reasons to believe that using the pixel dichotomy model at moderate spatial resolutions (250 m) is a less appropriate choice for monitoring grassland cover in large areas when comparable accuracy of the prediction results is required.

4.2. Comparison of the suitability of NDVI and EVI for modeling grassland cover

Previous studies showed that EVI is different from NDVI because it attempts to correct the influence of the atmosphere and soil background

and keeps the regular VI value distribution under the high biomass region (Huete et al., 2000; Ahmad, 2012). Correlation analyses between alpine grassland cover and several VIs were conducted by Liu et al. (2014), and they proved that EVI was better than NDVI in reflecting the change in grassland vegetation cover on the southwestern Tibetan Plateau. The grassland cover regression model based on EVI (RMSE = 6.77%) also displayed a lower error than the NDVI-based model (RMSE = 7.61%). Similar results were obtained from a study of alpine grassland cover in Gansu province, located on the northeastern Tibetan Plateau (Meng et al., 2018). However, the NDVI outperforms the EVI for estimating alpine grassland cover in our study. Chen et al. (2016) obtained the same results in a study on FVC in an alpine grassland on the northeastern edge of the Tibetan Plateau. Thus, EVI is not necessarily superior to NDVI for deriving vegetation cover, although it is an “optimized index”. Although the research object of all above studies was the alpine grassland cover of the Tibetan Plateau, the specific study areas of these studies were different, with different environmental conditions. Moreover, in natural grasslands, there are great changes in vegetation composition in different regions; therefore, the growth status and vegetation types might explain why NDVI is more suitable for deriving grassland cover than EVI. In addition, EVI mainly solves the problem of the tendency of NDVI to be saturated in high-biomass areas. The mean NDVI value obtained in this study is 0.61, and the phenomenon of NDVI saturation did not occur as shown in Fig. 2. In the study by Liang et al. (2016), the results showed that NDVI presented a higher correlation with grassland aboveground biomass than EVI in the Qingnan pasture region, which is a similar, but larger research area than the HRHR. Overall, it seems that NDVI is a more suitable VI than EVI in modeling grassland vegetation cover in the HRHR.

4.3. Factors affecting the accuracy of the optimal model

The SVM model is proved to exhibit higher stability and better predictive power than the other models established in this study, although some problems remain. First, spatial inconsistencies still occur between the sample plots and the satellite data, even the sample plot of 100 m × 100 m is used (and it is better than the traditional 5 sub-plots of 0.5 m × 0.5 m or 1 m × 1 m), it is still smaller than the 250 m × 250 m of MODIS data. This disparity inevitably introduces errors during model establishment. However, the problem is difficult to solve because it is unrealistic to identify a large number of sample plots in the grassland community of the HRHR with relatively flat terrain, a

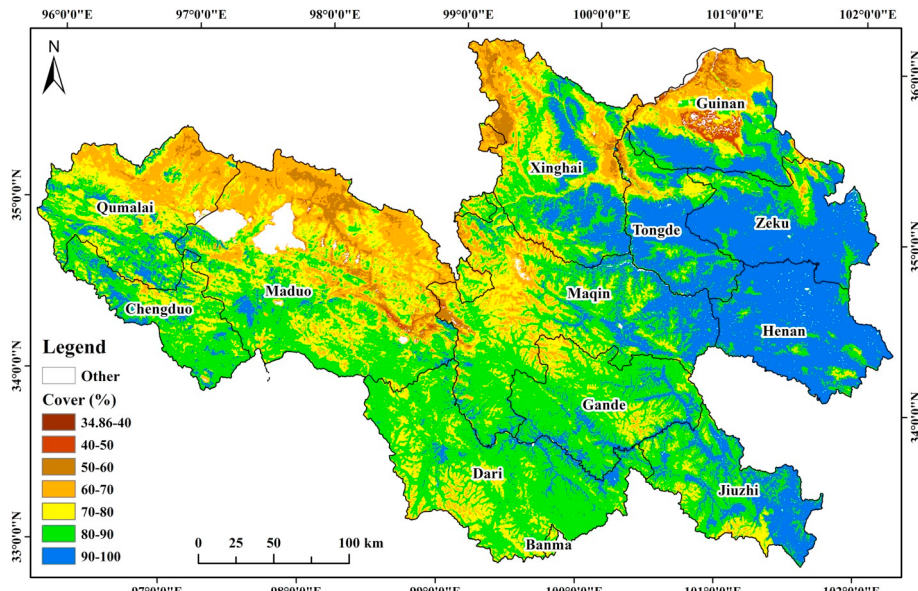


Fig. 4. Spatial distribution map of average yearly maximum grassland cover at the pixel scale (250 m) in the HRHR from 2001 to 2016.

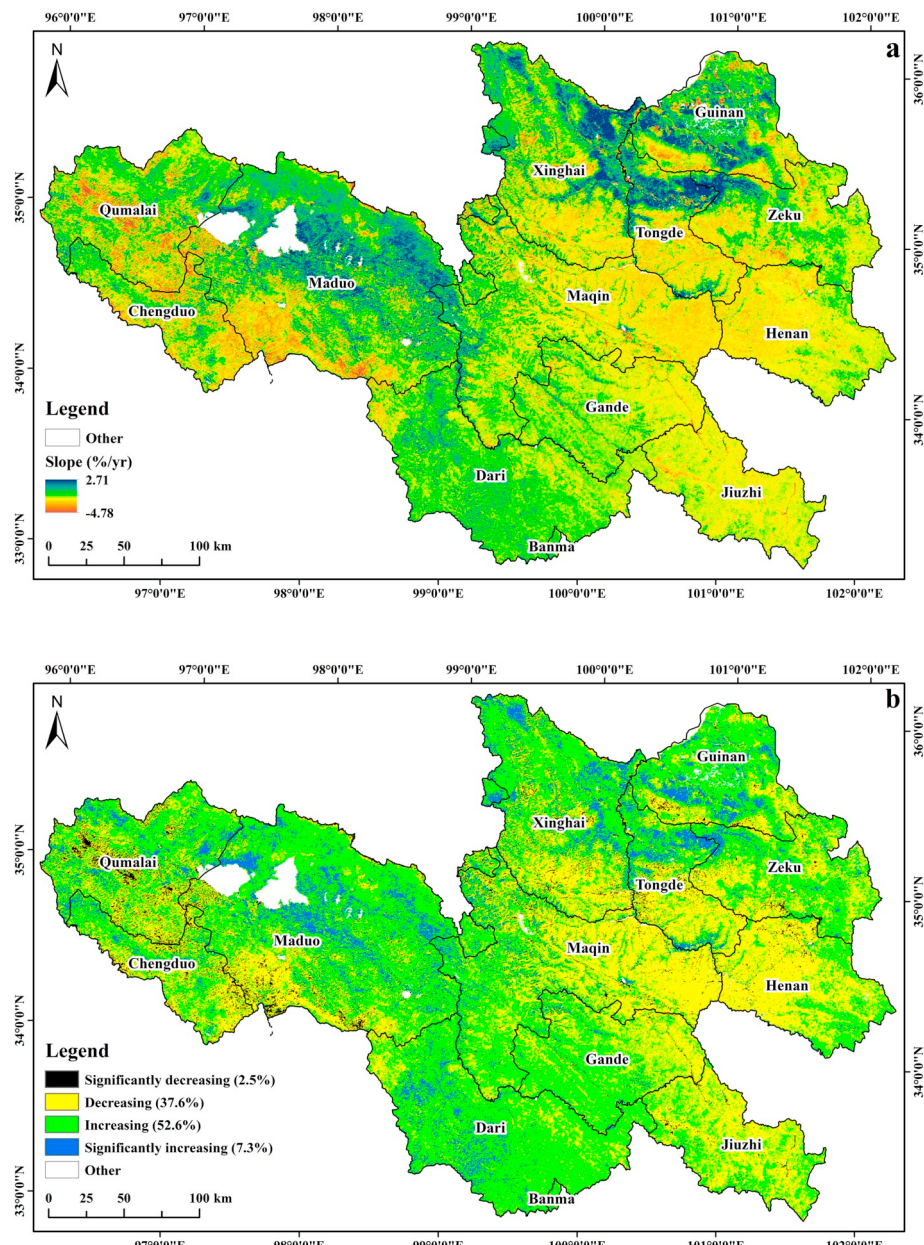


Fig. 5. Change trend of yearly maximum grassland cover at the pixel scale (250 m) (a) and the corresponding grading result (b) in the HRHR from 2001 to 2016.

uniform growth status and a size of 250 m × 250 m. Ideally, each plot also needs to be perfectly consistent with a single MODIS pixel in terms of spatial location.

Second, the accuracy of the geographic location, topography, soil and meteorology factors used in this study impact the SVM model, particularly the climate data. Previous studies indicated that climate factors strongly correlate with grassland growth (Wang et al., 2016; Guo et al., 2008). However, in our study, the precipitation and temperature are only moderately associated with grassland cover, possibly due to insufficient number of meteorological stations.

Third, although the SVM model is recognized as a valuable tool for dealing with small samples and nonlinear regressions, and the predicted results of the SVM model are highly correlated with predictor variables, the model has its own limitations. The performance of an SVM is affected by its parameters and kernel function, where a small value of the kernel width parameter may lead to overfitting, while a large value of the kernel width parameter may cause over-smoothing (Mountrakis et al., 2011). However, it is difficult to select the optimal kernel

function and parameters for the SVM model in practice. The present comparatively mature kernel functions and its parameters are selected based on personal experiences, such as the RBF kernel function used in this study. This is to say that the parameters are adjusted repeatedly in this study to achieve better model performance. However, we still cannot guarantee that the result is the optimal solution. In addition, SVMs have deficit in addressing the common problem of noise, which often exists in satellite images. Due to the limitation of satellite image sensors and the influence of topographic and atmospheric distortions, the MODIS-derived VIs themselves present systematic errors. Additionally, the performance of the SVM model is affected by the support vectors, i.e., not all training samples can become support vectors. However, it is impossible to ensure that all measured data of grassland cover in the field survey can act as support vectors of the SVM model. Therefore, with an increasing sample size in the future, other machine learning algorithms (such as DT and ANN) can be further explored.

5. Conclusions

This study assesses the stability and accuracy of four types of grassland cover models, based on the UAV-measured grassland cover data and MODIS VI products in the HRHR during the period of 2014 to 2016. The SVM model is found to be the optimal model, while the pixel dichotomy model is the worst. It is also interesting to find that the NDVI-based models outperform the EVI-based models, for both pixel dichotomy models and univariate VI regression models. Nine factors are selected in building the multivariate regression models and the SVM model, with NDVI as the most relevant factor. Based on the SVM model, the average yearly maximum grassland cover from 2001 to 2016 exhibited a general trend of increasing from the west to east and from north to south. Over the 16 years period, it is found that grasslands in the HRHR showed more increase than decrease in grassland cover (59.9% vs. 40.1%). In particular, the majority of areas with significant increase in grassland cover were located in the low grass cover zones, while the majority of areas with decrease in grassland cover were found in the high grass cover zones.

Acknowledgments

We are very grateful for the valuable comments and suggestions from the Associate Editor and reviewers to significantly improve the paper. This study was supported by the Program for Changjiang Scholars and Innovative Research Team in Universities (IRT_17R50), the National Natural Science Foundation of China (31672484, 31372367, 31702175 and 41671330), and the Consulting Project of the Engineering Academy of China (2018-XZ-25).

References

Ahmad, F., 2012. A review of remote sensing data change detection: comparison of Faisalabad and Multan districts, Punjab province, Pakistan. *J Planning*. 5 (9), 236–251.

Bauer, K., Nyima, Y., 2011. Laws and regulations impacting the enclosure movement on the Tibetan Plateau of China. *Himalaya* 30 (1), 23–37.

Benoit, D.F., Van den Poel, D., 2009. Benefits of quantile regression for the analysis of customer lifetime value in a contractual setting: an application in financial services. *Expert Syst. Appl.* 36 (7), 10475–10484.

Beurs, K.M.D., Henebry, G.M., 2004. Land surface phenology, climatic variation, and institutional change: analyzing agricultural land cover change in Kazakhstan. *Remote Sens. Environ.* 89 (4), 497–509.

Boyd, D.S., Foody, G.M., Ripple, W.J., 2002. Evaluation of approaches for forest cover estimation in the Pacific northwest, USA, using remote sensing. *Appl. Geogr.* 22 (4), 375–392.

Camps-Valls, G., Bruzzone, L., Rojo-Alvarez, J.L., Melgani, F., 2006. Robust support vector regression for biophysical variable estimation from remotely sensed images. *IEEE Geosci. Remote Sens. Lett.* 3 (3), 339–343.

Capolupo, A., Kooistra, L., Berendonk, C., Boccia, L., Suomalainen, J., 2015. Estimating plant traits of grasslands from UAV-acquired hyperspectral images: a comparison of statistical approaches. *Int. J. Geogr. Inf. Sci.* 4 (4), 2792–2820.

Carlson, T.N., Ripley, D.A., 1997. On the relation between NDVI, fractional vegetation cover, and leaf area index. *Remote Sens. Environ.* 62 (3), 241–252.

Chang, C.C., Lin, C.J., 2011. LIBSVM: a library for support vector machines. *ACM Trans. Intell. Syst. Technol.* 2 (3), 1–27.

Chen, J.J., Yi, S.H., Qin, Y., Wang, X.Y., 2016. Improving estimates of fractional vegetation cover based on UAV in alpine grassland on the Qinghai-Tibetan Plateau. *Int. J. Remote Sens.* 37 (8), 1922–1936.

Chu, H.B., Wei, J.H., Li, T.J., Jia, K., 2016. Application of support vector regression for mid-and long-term runoff forecasting in “Yellow River Headwater” Region. *Procedia Eng.* 154, 1251–1257.

Colomina, I., Molina, P., 2014. Unmanned aerial systems for photogrammetry and remote sensing: a review. *ISPRS J. Photogramm. Remote Sens.* 92 (2), 79–97.

Dai, S.P., Zhang, B., Wang, H.J., Wang, Y.M., Guo, L.X., Wang, X.M., Li, D., 2011. Vegetation cover change and the driving factors over northwest China. *J. Arid. Land* 3 (1), 25–33.

Delamerat, P.L., Messina, J.P., Qi, J., Cochrane, M.A., 2012. A hybrid visual estimation method for the collection of ground truth fractional coverage data in a humid tropical environment. *Int. J. Appl. Earth Obs. Geoinf.* 18, 504–514.

Elmore, A.J., Mustard, J.F., Manning, S.J., Lobell, D.B., 2000. Quantifying vegetation change in semiarid environments: precision and accuracy of spectral mixture analysis and the normalized difference vegetation index. *Remote Sens. Environ.* 73 (1), 87–102.

Feng, J.M., Wang, T., Qi, S.Z., Xie, C.W., 2005. Land degradation in the source region of the Yellow River, northeast Qinghai-Xizang Plateau: classification and evaluation. *Environ. Geol.* 47 (4), 459–466.

Fensholt, R., Rasmussen, K., Nielsen, T.T., Mbow, C., 2009. Evaluation of earth observation based long term vegetation trends—Intercomparing NDVI time series trend analysis consistency of Sahel from AVHRR GIMMS, Terra MODIS and SPOT VGT data. *Remote Sens. Environ.* 113 (9), 1886–1898.

Flynn, K.F., Chapra, S.C., 2014. Remote sensing of submerged aquatic vegetation in a shallow non-turbid river using an unmanned aerial vehicle. *Remote Sens.* 6 (12), 12815–12836.

Foody, G.M., Mathur, A., 2004. Toward intelligent training of supervised image classifications: directing training data acquisition for SVM classification. *Remote Sens. Environ.* 93 (1), 107–117.

Gao, T., Yang, X.C., Jin, Y.X., Ma, H.L., Li, J.Y., Yu, H.D., Yu, Q.Y., Zheng, X., Xu, B., 2013. Spatio-temporal variation in vegetation biomass and its relationships with climate factors in the Xilingol grasslands, northern China. *PLoS One* 8 (12), 1–10.

Gitelson, A.A., Kaufman, Y.J., Stark, R., Rundquist, D., 2002. Novel algorithms for remote estimation of vegetation fraction. *Remote Sens. Environ.* 80 (1), 76–87.

Goetz, S.J., Wright, R.K., Smith, A.J., Zinecker, E., Schaub, E., 2003. IKONOS imagery for resource management: tree cover, impervious surfaces, and riparian buffer analyses in the mid-Atlantic region. *Remote Sens. Environ.* 88 (1), 195–208.

Guerschman, J.P., Hill, M.J., Renzullo, L.J., Barrett, D.J., Marks, A.S., Botha, E.J., 2009. Estimating fractional cover of photosynthetic vegetation, non-photosynthetic vegetation and bare soil in the Australian tropical savanna region upscaling the EO-1 Hyperion and MODIS sensors. *Remote Sens. Environ.* 113 (5), 928–945.

Guo, W.Q., Yang, T.B., Dai, J.G., Shi, L., Lu, Z.Y., 2008. Vegetation cover changes and their relationship to climate variation in the source region of the Yellow River, China, 1990–2000. *Int. J. Remote Sens.* 29 (7), 2085–2103.

Gutman, G., Ignatov, A., 1998. The derivation of the green vegetation fraction from NOAA/AVHRR data for use in numerical weather prediction models. *Int. J. Remote Sens.* 19 (8), 1533–1543.

Hansen, M.C., Defries, R.S., Townshend, J.R.G., Marufu, L., Sohlberg, R., 2002a. Development of a MODIS tree cover validation data set for Western Province, Zambia. *Remote Sens. Environ.* 83 (1–2), 320–335.

Hansen, M.C., Defries, R.S., Townshend, J.R.G., Sohlberg, R., Dimiceli, C., Carroll, M., 2002b. Towards an operational MODIS continuous field of percent tree cover algorithm: examples using AVHRR and MODIS data. *Remote Sens. Environ.* 83 (1), 303–319.

Hu, Y., Maskey, S., Uhlenbrook, S., 2012. Trends in temperature and rainfall extremes in the Yellow River source region, China. *Clim. Chang.* 110 (1–2), 403–429.

Hu, G.Y., Yu, L.P., Dong, Z.B., Jin, H.J., Luo, D.L., Wang, Y.X., Lai, Z.P., 2017. Holocene aeolian activity in the headwater region of the Yellow River, northeast Tibet Plateau, China: a first approach by using OSL-dating. *Catena* 149, 150–157.

Huete, A., Justice, C.O., Liu, H.Q., 1994. Development of vegetation and soil indices for MODIS-EOS. *Remote Sens. Environ.* 49 (3), 224–234.

Huete, A., Liu, H.Q., Batchily, K., Leeuw, W.V., 1997. A comparison of vegetation indices over a global set of TM images for EOS-MODIS. *Remote Sens. Environ.* 59 (3), 440–451.

Huete, A., Didan, K., Shimabukuro, Y., Ferreira, L., Rodriguez, E., 2000. Regional Amazon basin and global analyses of MODIS vegetation indices: early results and comparisons with AVHRR. *IEEE Trans. Geosci. Remote Sens.* 16 (2), 536–538.

Huete, A., Didan, K., Miura, T., Rodriguez, E.P., Gao, X., Ferreira, L.G., 2002. Overview of the radiometric and biophysical performance of the MODIS vegetation indices. *Remote Sens. Environ.* 83 (1), 195–213.

Hutchinson, M.F., 2006. ANUSPLIN version 4.36 user guide. Australian National University, Canberra, 2006.

Jakubauskas, M., Kindscher, K., Fraser, A., Debinski, D., Price, K.P., 2000. Close-range remote sensing of aquatic macrophyte vegetation cover. *Int. J. Remote Sens.* 21 (18), 3533–3538.

Jamieson, P.D., Porter, J.R., Wilson, D.R., 1991. A test of computer simulation model ARC-WHEAT1 on wheat crops grown in New Zealand. *Field Crop Res.* 27 (4), 337–350.

Jaipaer, G., Chen, X., Bao, A., 2011. A comparison of methods for estimating fractional vegetation cover in arid regions. *Agric. For. Meteorol.* 151 (12), 1698–1710.

Jin, H.J., Luo, D.L., Wang, S.L., Lü, L.Z., Wu, J.C., 2011. Spatiotemporal variability of permafrost degradation on the Qinghai-Tibet Plateau. *Sci. Cold Arid Reg.* 3 (4), 281–305.

Kaufman, Y.J., Tanré, D., 1992. Atmospherically resistant vegetation index (ARVI) for EOS-MODIS. *IEEE Trans. Geosci. Remote Sens.* 30 (2), 261–270.

Kergoat, L., Hiernaux, P., Dardel, C., Pierre, C., Guiachard, F., Kalilou, A., 2015. Dry-season vegetation mass and cover fraction from SWIR1.6 and SWIR2.1 band ratio: ground-radiometer and MODIS data in the Sahel. *Int. J. Appl. Earth Obs. Geoinf.* 39, 56–64.

Lehnert, L.W., Meyer, H., Wang, Y., Miehe, G., Thies, B., Reudenbach, C., Bendix, J., 2015. Retrieval of grassland plant coverage on the Tibetan Plateau based on a multi-scale, multi-sensor and multi-method approach. *Remote Sens. Environ.* 164, 197–207.

Li, Z.Q., Guo, X.L., 2014. Topographic effects on vegetation biomass in semiarid mixed grassland under climate change using AVHRR NDVI data. *Bri. J. Environ. Clim. Change* 4 (2), 229–242.

Li, F., Chen, W., Zeng, Y., Zhao, Q.J., Wu, B.F., 2014. Improving estimates of grassland fractional vegetation cover based on a pixel dichotomy model: a case study in Inner Mongolia, China. *Remote Sens.* 6 (6), 4705–4722.

Li, Q., Yang, M.X., Wan, G.N., Wang, X.J., 2016. Spatial and temporal precipitation variability in the source region of the Yellow River. *Environ. Earth Sci.* 75 (7), 594.

Liang, T.G., Yang, S.X., Feng, Q.S., Liu, B.K., Zhang, R.P., Huang, X.D., Xie, H.J., 2016. Multi-factor modeling of above-ground biomass in alpine grassland: a case study in the Three-River Headwaters Region, China. *Remote Sens. Environ.* 186, 164–172.

Liu, L.S., Zhang, Y.L., Bai, W.Q., Yan, J.Z., Ding, M.J., Shen, Z.X., Li, S.C., Zheng, D., 2006.

Characteristics of grassland degradation and driving forces in the source region of the Yellow River from 1985 to 2000. *J. Geogr. Sci.* 16 (2), 131–142.

Liu, L.Y., Jing, X., Wang, J.H., Zhao, C.J., 2009. Analysis of the changes of vegetation coverage of western Beijing mountainous areas using remote sensing and GIS. *Environ. Monit. Assess.* 153 (1–4), 339–349.

Liu, B., Shen, W.S., Lin, N.F., Li, R., Yue, Y.M., 2014. Deriving vegetation fraction information for the alpine grassland on the Tibetan Plateau using *in situ* spectral data. *J. Appl. Remote. Sens.* 8 (17), 1–17.

Loague, K., Green, R.E., 1991. Statistical and graphical methods for evaluating solute transport models: overview and application. *J. Contam. Hydrol.* 7 (1–2), 51–73.

Mbogga, M.S., Hamann, A., Wang, T.L., 2009. Historical and projected climate data for natural resource management in western Canada. *Agric. For. Meteorol.* 149 (5), 881–890.

McVicar, T.R., Van Niel, T.G., Li, L.T., Hutchinson, M.F., Mu, X.M., Liu, Z.H., 2007. Spatially distributing monthly reference evapotranspiration and pan evaporation considering topographic influences. *J. Hydrol.* 338 (3–4), 196–220.

Meng, B.P., Gao, J.L., Liang, T.G., Cui, X., Ge, J., Yin, J.P., Feng, Q.S., Xie, H.J., 2018. Modeling of alpine grassland cover based on unmanned aerial vehicle technology and multi-factor methods: a case study in the east of Tibetan Plateau, China. *Remote Sens.* 10 (2), 320.

Mountakis, G., Im, J., Ogole, C., 2011. Support vector machines in remote sensing: a review. *ISPRS J. Photogramm. Remote Sens.* 66 (3), 247–259.

North, P.R.J., 2002. Estimation of f_{APAR} , LAI, and vegetation fractional cover from ATSR-2 imagery. *Remote Sens. Environ.* 80 (1), 114–121.

O'Connor, T.G., Haines, L.M., Snyman, H.A., 2001. Influence of precipitation and species composition on phytomass of a semi-arid African grassland. *J. Ecol.* 89 (5), 850–860.

Okin, G.S., Clarke, K.D., Lewis, M.M., 2013. Comparison of methods for estimation of absolute vegetation and soil fractional cover using MODIS normalized BRDF-adjusted reflectance data. *Remote Sens. Environ.* 130 (130), 266–279.

Olden, J.D., Jackson, D.A., 2000. Torturing data for the sake of generality: how valid are our regression models? *Ecoscience* 7 (4), 501–510.

Pan, J., Zhu, Y., Cao, W.X., Dai, T.B., Jiang, D., 2006. Predicting the protein content of grain in winter wheat with meteorological and genotypic factors. *Plant Prod. Sci.* 9 (3), 323–333.

Patel, N.K., Saxena, R.K., Shiwalkar, A., 2007. Study of fractional vegetation cover using high spectral resolution data. *J. Indian Soc. Remote Sens.* 35 (1), 73–79.

Price, D.T., McKenney, D.W., Nalder, I.A., Hutchinson, M.F., Kesteven, J.L., 2000. A comparison of two statistical methods for spatial interpolation of Canadian monthly mean climate data. *Agric. For. Meteorol.* 101 (2–3), 81–94.

Psomas, A., Kneubühler, M., Huber, S., Itten, K., Zimmermann, N.E., 2011. Hyperspectral remote sensing for estimating aboveground biomass and for exploring species richness patterns of grassland habitats. *Int. J. Remote Sens.* 32 (24), 9007–9031.

Purevdorj, T.S., Tateishi, R., Ishiyama, T., Honda, Y., 1998. Relationships between percent vegetation cover and vegetation indices. *Int. J. Remote Sens.* 19 (18), 3519–3535.

Qi, J., Marssett, R.C., Moran, M.S., Goodrich, D.C., Heilman, P., Kerr, Y.H., Dedieu, G., Chehbouni, A., Zhang, X.X., 2000. Spatial and temporal dynamics of vegetation in the San Pedro River basin area. *Agric. For. Meteorol.* 105 (1–3), 55–68.

Qin, R.J., 2014. An object-based hierarchical method for change detection using unmanned aerial vehicle images. *Remote Sens.* 6 (9), 7911–7932.

Rango, A., Laliberte, A., Steele, C., Herrick, J.E., Bestelmeyer, B., Schmugge, T., Roanhorse, A., Jenkins, V., 2006. Using unmanned aerial vehicles for rangelands: current applications and future potentials. *Environ. Pract.* 8 (3), 159–168.

Rango, A., Laliberte, A., Herrick, J.E., Winters, C., Havstad, K., Steele, C., Browning, D., 2009. Unmanned aerial vehicle-based remote sensing for rangeland assessment, monitoring, and management. *J. Appl. Remote. Sens.* 3 (1), 1–15.

Rinaldi, M., Losavio, N., Flagella, Z., 2003. Evaluation and application of the OILCROP-SUN model for sunflower in southern Italy. *Agric. Syst.* 78 (1), 17–30.

Rundquist, B.C., 2002. The influence of canopy green vegetation fraction on spectral measurements over native tallgrass prairie. *Remote Sens. Environ.* 81 (1), 129–135.

Salamí, E., Barrado, C., Pastor, E., 2014. UAV flight experiments applied to the remote sensing of vegetated areas. *Remote Sens.* 6 (11), 11051.

Schwieder, M., Leitão, P.J., Sues, S., Senf, C., Hostert, P., 2014. Estimating fractional shrub cover using simulated EnMAP data: a comparison of three machine learning regression techniques. *Remote Sens.* 6 (4), 3427–3445.

Song, Y., Ma, M.G., Veroustraete, F., 2010. Comparison and conversion of AVHRR GIMMS and SPOT vegetation NDVI data in China. *Int. J. Remote Sens.* 31 (9), 2377–2392.

Stow, D.A., Hope, A., McGuire, D., Verbyla, D., Gamon, J., Huemmrich, F., Houston, S., Racine, C., Sturm, M., Tape, K., Hinzman, L., Yoshikawa, K., Tweedie, C., Noyel, B., Silapaswan, C., Douglas, D., Griffith, B., Jia, G.S., Epstein, H., Walker, D., Daeschner, S., Petersen, A., Zhou, L.M., Myneni, R., 2004. Remote sensing of vegetation and land-cover change in arctic tundra ecosystems. *Remote Sens. Environ.* 89 (3), 281–308.

Tucker, C.J., Justice, C.O., Prince, S.D., 1986. Monitoring the grasslands of the Sahel 1984–1985. *Int. J. Remote Sens.* 7 (11), 1571–1581.

Vapnik, V., Golowich, S.E., Smola, A., 1996. Support vector method for function approximation, regression estimation, and signal processing. *Adv. Neural Inf. Proces. Syst.* 9, 281–287.

Verrelst, J., Camps-Valls, G., Muñoz-Marí, J., Rivera, J.P., Veroustraete, F., Clevers, J.G.P.W., Moreno, J., 2015. Optical remote sensing and the retrieval of terrestrial vegetation bio-geophysical properties—a review. *ISPRS J. Photogramm. Remote Sens.* 108, 273–290.

Wang, J., Price, K.P., Rich, P.M., 2001. Spatial patterns of NDVI in response to precipitation and temperature in the central great plains. *Int. J. Remote Sens.* 22 (18), 3827–3844.

Wang, H.M., Sun, J., Li, W.P., Wu, J.B., Chen, Y.J., Liu, W.H., 2016. Effects of soil nutrients and climate factors on belowground biomass in an alpine meadow in the source region of the Yangtze-Yellow Rivers, Tibetan Plateau of China. *J. Arid. Land* 8 (6), 881–889.

Wang, P., Deng, X.Z., Jiang, S.J., 2017. Diffused impact of grassland degradation over space: a case study in Qinghai province. *Phys. Chem. Earth* 101, 166–171.

Wei, S.G., Dai, Y.J., Liu, B.Y., Ye, A.Z., Yuan, H., 2012. A soil particle-size distribution dataset for regional land and climate modelling in China. *Geoderma* 171–172 (1), 85–91.

Wittich, K.P., Hansing, O., 1995. Area-averaged vegetative cover fraction estimated from satellite data. *Int. J. Biometeorol.* 38 (4), 209–215.

Wu, C.S., Murray, A.T., 2003. Estimating impervious surface distribution by spectral mixture analysis. *Remote Sens. Environ.* 84 (4), 493–505.

Xiao, J.F., Moody, A., 2005. A comparison of methods for estimating fractional green vegetation cover within a desert-to-upland transition zone in central New Mexico, USA. *Remote Sens. Environ.* 98 (2–3), 237–250.

Yang, S.X., Feng, Q.S., Liang, T.G., Liu, B.K., Zhang, W.J., Xie, H.J., 2017. Modeling grassland above-ground biomass based on artificial neural network and remote sensing in the Three-River Headwaters Region. *Remote Sens. Environ.* 204, 448–455.

Yeh, E.T., 2005. Green governmentality and pastoralism in western China: ‘Converting pastures to grasslands’. *Nomadic Peoples* 9 (1–2), 9–30.

Yi, S.H., 2017. FragMAP: a tool for long-term and cooperative monitoring and analysis of small-scale habitat fragmentation using an unmanned aerial vehicle. *Int. J. Remote Sens.* 38 (8–10), 2686–2697.

Yi, S.H., Chen, J.J., Qin, Y., Xu, G.W., 2016. The burying and grazing effects of plateau pika on alpine grassland are small: a pilot study in a semiarid basin on the Qinghai-Tibet plateau. *Biogeosciences* 13 (22), 6273–6284.

Yu, M.C., 2011. Multi-criteria ABC analysis using artificial-intelligence-based classification techniques. *Expert Syst. Appl.* 38 (4), 3416–3421.

Yu, G.A., Brierley, G., Huang, H.Q., Wang, Z.Y., Blue, B., Ma, Y.X., 2014. An environmental gradient of vegetative controls upon channel planform in the source region of the Yangtze and Yellow Rivers. *Catena* 119 (119), 143–153.

Zeng, X.B., Dickinson, R.E., Walker, A., Shaikh, M., Defries, R.S., Qi, J.G., 2000. Derivation and evaluation of global 1-km fractional vegetation cover data for land modeling. *J. Appl. Meteorol.* 39 (6), 826–839.

Zha, Y., Gao, J., Ni, S.X., Liu, Y.S., Jiang, J.J., Wei, Y.C., 2003. A spectral reflectance-based approach to quantification of grassland cover from Landsat TM imagery. *Remote Sens. Environ.* 87 (2–3), 371–375.

Zhao, H.D., Liu, S.L., Dong, S.K., Su, X.K., Wang, X.X., Wu, X.Y., Wu, L., Zhang, X., 2015. Analysis of vegetation change associated with human disturbance using MODIS data on the rangelands of the Qinghai-Tibet Plateau. *Rangeland J.* 37 (1), 77–87.

Zhou, Q., Robson, M., 2001. Automated rangeland vegetation cover and density estimation using ground digital images and a spectral-contextual classifier. *Int. J. Remote Sens.* 22 (17), 3457–3470.

Zhou, H.K., Zhao, X.Q., Tang, Y.H., Gu, S., Zhou, L., 2005. Alpine grassland degradation and its control in the source region of the Yangtze and Yellow Rivers, China. *Grassl. Sci.* 51 (3), 191–203.

Zribi, M., Hégarat-Mascle, S.L., Taconet, O., Ciarletti, V., Vidal-Madjar, D., Boussemra, M.R., 2003. Derivation of wild vegetation cover density in semi-arid regions: ERS2/SAR evaluation. *Int. J. Remote Sens.* 24 (6), 1335–1352.